Thin Solid Films 519 (2011) 3897–3901

Contents lists available at ScienceDirect

Thin Solid Films

journal homepage: www.elsevier.com/locate/tsf

Influence of hydrogen plasma treatment on charge storage characteristics in high density tungsten nanocrystal nonvolatile memory

Shih-Cheng Chen [a], Ting-Chang Chang [b,*], Wei-Ren Chen [c], Yuan-Chun Lo [d], Kai-Ting Wu [d], S.M. Sze [c], Jason Chen [e], I.H. Liao [e], Fon-Shan Yeh(Huang) [a]

[a] Department of Electrical Engineering & Institute of Electronic Engineering, National Tsing Hua University, Taiwan
[b] Department of Physics and Institute of Electro-Optical Engineering, and Center for Nanoscience and Nanotechnology, National Sun Yat-Sen University, Taiwan
[c] Institute of Electronics, National Chiao Tung University, Hsin-Chu, Taiwan
[d] Institute Photonics of Technologies National Tsing Hua University, Taiwan
[e] ProMOS Technologies, No. 19 Li Hsin Rd., Science-Based Industrial Park, Hsinchu, Taiwan

ARTICLE INFO

Article history:
Received 14 July 2010
Received in revised form 12 January 2011
Accepted 14 January 2011
Available online 27 January 2011

Keywords:
Hydrogen plasma
Tungsten nanocrystals
Nonvolatile memory
X-ray photoelectron spectroscopy

ABSTRACT

This study focuses on the influence of a hydrogen plasma treatment on electrical properties of tungsten nanocrystal nonvolatile memory. The X-ray photon emission spectra show that, after the hydrogen plasma treatment, a change in binding energy occurs such that Si^{x+} and Si^{y+} peaks appear at a position that is shifted about 2.3 and 3.3 eV from Si^{0+} in Si 2p spectra. This indicates that Si dangling bonds are passivated to form a Si–H bond structure in the SiO_2. Furthermore, the transmission electron microscopy shows cross-sectional and plane-view for the nanocrystal microstructure after the hydrogen plasma treatment. Electrical measurement analyses show improved data retention because the hydrogen plasma treatment enhances the quality of the oxide surrounding the nanocrystals. The endurance and retention properties of the memory device are improved by about 36% and 30%, respectively.

© 2011 Elsevier B.V. All rights reserved.

1. Introduction

Conventional nonvolatile memory (NVM, flash memory) suffers from certain limitations during continual scaling of device structures [1]. Therefore, in recent years nanocrystal (NC) nonvolatile memory devices have been investigated as a method to overcome these drawbacks. Because discrete trap storage nodes act as the charge center of NC nonvolatile memory devices, they can effectively avoid data loss in terms of reliability when scaling down such devices [2].

Among various NC nonvolatile memories [3–5], metal NCs are good candidates for improving the retention property and charge storage ability [6] due to their high work function, which provides a lower potential well compared to the silicon substrate. Tungsten (W) NC was chosen because, besides its high work function (4.9 eV), thermal stability is suitable for the process thermal budget [7–9]. Moreover, for nanoscale devices, the density of nanocrystals is an issue because the memory window is dependent on the NC density. High density is helpful to scale down the device structure. However, if the density of NCs is very high, then the quality of the oxide which surrounds the NCs will be critical because the electrons stored in NCs will escape easily by trap tunneling if the oxide quality is not sufficient. When NCs are very close to each other [10,11], there is a tradeoff between high NC density and good reliability for nano-NVM application. In order to achieve both high density and good reliability, using high-pressure hydrogen treatment with high temperature annealing (700–900 °C) has proven to be a valid method to improve the oxide surrounding NCs [12,13]. Unfortunately, metal NCs and metal control gates cannot endure this temperature treatment. Hence, a hydrogen plasma treatment is proposed for W NC nonvolatile memory as an alternative method to passivate the defects in the surrounding oxide and improve its quality. The advantages of this method are a simple fabrication process and a low thermal budget.

2. Experiment

The process flow and the memory structure for this study are shown in Fig. 1. The W NC NVM capacitor structure was fabricated on single-crystal 6 in. (100) oriented P-type silicon. After the standard RCA cleaning, wafers went through a thermal oxidative process in an atmospheric pressure chemical vapor deposition furnace to form a 5 nm thick dry SiO_2 layer that serves as a tunnel oxide. Afterward, a 4 nm thick tungsten silicide (WSi_2) thin film was deposited onto the tunnel oxide by sputtering at room temperature with argon plasma 50 sccm (sccm denotes cubic centimeter per minute at standard temperature and pressure) and a DC power of 100 W. Subsequently, a 6 nm thick amorphous silicon (a-Si) layer was deposited by the same system with argon plasma 30 sccm and a RF power of 100 W. After the deposition of this WSi_2/a-Si double layer structure, high temperature

* Corresponding author. Tel.: +886 7 5252000x3708; fax: +886 7 5253709.
E-mail address: tcchang@mail.phys.nsysu.edu.tw (T.-C. Chang).

0040-6090/$ – see front matter © 2011 Elsevier B.V. All rights reserved.
doi:10.1016/j.tsf.2011.01.259

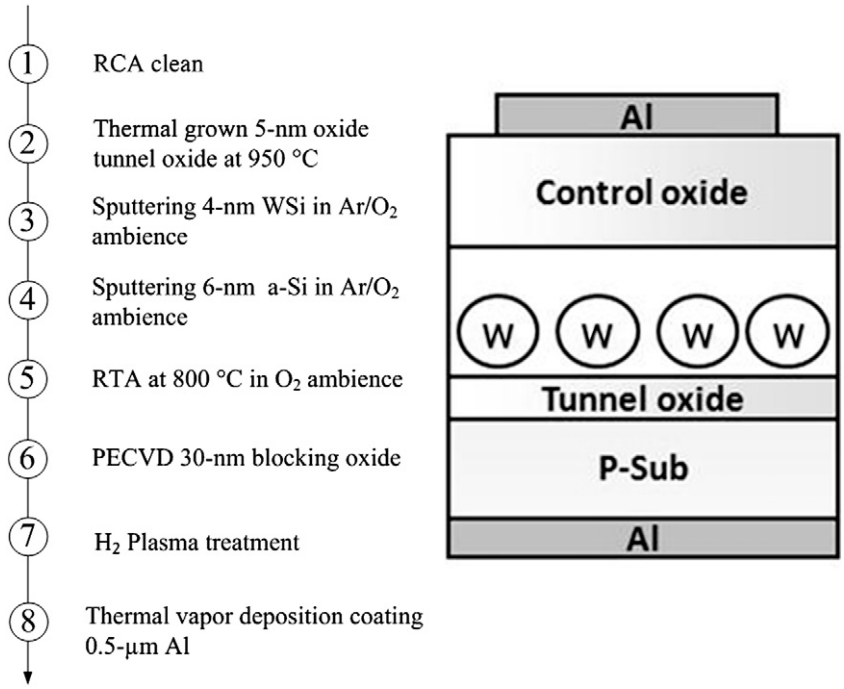

Fig. 1. Process flow and W nanocrystal NVM structure.

thermal oxidation was performed in the Rapid Thermal Annealing (RTA) system in oxygen ambient. RTA oxidation at 800 °C for 60 s is required to allow the WSi_2 layer to form W NCs, which then embed between the tunnel oxide and the control oxide. Afterwards, a 30 nm thick SiO_2 layer was deposited by a plasma enhanced chemical vapor deposition system to form a control oxide layer. For comparison, some of the samples were treated with hydrogen plasma for 30 min by high density plasma chemical vapor deposition at 200 W of plasma power and 200 sccm gas flow rate at 300 °C. The standard sample was plasma treated, whereas the control sample was used as reference without treatment, and will be referred to as standard and control samples hereafter. Finally, the top and the bottom Al electrodes were patterned by a shadow mask to form a metal–oxide–insulator–oxide–silicon structure. The aluminum was deposited by a thermal evaporator system with a thickness of 500 nm. Transmission electron microscope (TEM) analysis and X-ray photoelectron spectroscopy (XPS) were adopted for the microstructure and the chemical material analyses of nanoparticles. The cross-sectional TEM sample was prepared by focused ion beam process using a SII Nanotechnology Incorporated SMI 3050 system. The plane-view TEM sample was prepared by first polishing the sample thickness down to around 100 μm with a grinding polishing machine. Then the sample thickness is further reduced to about 10 μm by milling with Ar^+ ions using a Gatan Model 691 precise ion polishing system. The high-resolution TEM was carried out using a JEOL JEM-2100F system operated at 200 kV. XPS analysis was performed using a VG Scientific Microlab 310F with 300 W Al Kα (1486.6 eV) as the X-ray source and was calibrated by a C 1s peak at 284.5 eV. The functions used for deconvolution are naturally broad and can be approximated with finite Gaussian or Lorentzian shape or a combination by XPSPEAK41 software. The electrical characteristics of capacitance–voltage (C–V) hysteresis were also measured by an HP4284 Precision LCR Meter with a high frequency of 100 kHz.

3. Results and discussion

Fig. 2(a) and (b) shows the TEM image cross-sectional and plane-view for the proposed device. The TEM image analyses show that the average diameter of nanocrystals is approximately 8 nm and the area density can be estimated to be about $2.5\times10^{12}\,cm^{-2}$. After going through the process indicated above, a high density of NCs was gained appropriate for 32–22 nm device applications.

Fig. 3(a) and (b) shows the Si 2p spectra of the control and standard sample, performed by a monochromatic Al *Kα* (1486.6 eV) X-ray. In Fig. 3(a), the transition region spectra between Si^{0+} and Si^{4+} are not observed in the SiO_2, which had not been exposed to the hydrogen plasma. Therefore, deconvolution of the spectra was carried out assuming that only Si^{0+} and Si^{4+} peaks exist in the Si 2p spectra for the unexposed SiO_2 [14–17]. In contrast, the SiO_2 which had been exposed to the hydrogen plasma exhibited transition region spectra between Si^{0+} and Si^{4+} in the Si 2p spectra, shown in Fig. 3(b). These transition region spectra could not be deconvoluted as Si^{3+}, Si^{2+} and Si^{1+}. It has been reported that Si^{x+} and Si^{y+} spectra which have shifted about 2.3 and 3.3 eV from Si^{0+} will appear in Si 2p spectra if a Si–H bond structure exists in the SiO_2. Therefore, because our results exhibit just such transition spectra, the sample with hydrogen plasma treatment can be assumed to produce the Si–H bonding and chemical shifts for Si–H bonding configurations, as shown in Fig. 3(c). In addition, the shift to lower energy and the increase in the intensity of the Si^{0+} peak and the presence of the Si^{2+} after hydrogen plasma treatment are caused by the Si and Si–Si_2O_2 reduction from weak Si– O_4 bonds [18–20]. Moreover, W 4f core-level photoemission spectra of the control and standard samples both consist of the two main peaks of W $4f^{7/2}$ (31.4 eV) and W $4f^{5/2}$ (33.5 eV), as shown in Fig. 4(a) and (b). The small peak at a position 35.2 eV is the peak of WO_3 of W 4f bonding [21,22]. Some of the W was probably oxidized during the rapid thermal annealing in the oxygen ambient because the solid solubility of O atoms within W material is extremely small [23], and O atoms cannot exist in W nanocrystals except if there is absolute oxidation of tungsten. Therefore, the position of WO_3 will be on the surface of the W nanocrystals. The W 4f spectra of the control and standard sample are very similar. In addition, in our experiment, the hydrogen plasma treatment is a post-treatment after the W nanocrystal formation. Therefore, it is unlikely that the W 4f spectra of the control and standard sample would show major differences, as the treatment does not influence the W nanocrystal formation.

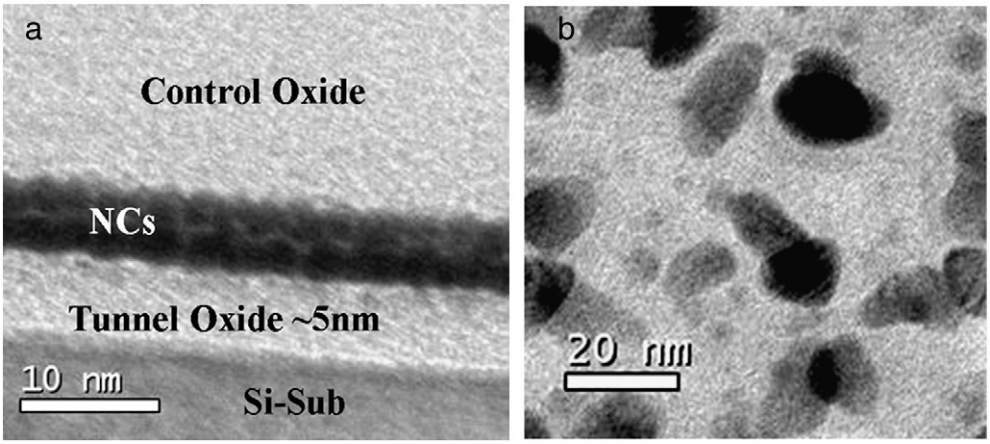

Fig. 2. TEM image of W nanocrystal NVM. (a) Cross-section, and (b) plane-view.

As the C–V hysteresis diagram in Fig. 5 shows, the memory window is ~8.8 V under ±10 V compared to the flat-band gate voltage operation. This memory window is sufficient to define the digital data information "1" and "0" for low power nano-NVM applications. Moreover, hysteresis loops follow a counterclockwise direction due to the injection of electrons from the inversion state and the discharge of electrons from the accumulation state of the Si substrate. The memory window of the standard sample that had the plasma treatment is slightly larger than the control sample under the same operation voltage. Hence, the charge storage ability of W NC NVMs is not influenced by the post-hydrogen plasma treatment in the standard sample. This shows that, for metallic NCs, most of the efficacious electron store in the W NCs rather than the surrounding oxide defects. In general, the memory window decreases as the trap density is reduced in SONOS-type memory. However, in nanocrystal memory, because charges are mainly stored in nanocrystals, there is no obvious variation in the memory window as the device is treated by hydrogen plasma treatment. The slight increase of memory window suggests that the improvement of oxide quality surrounding the nanocrystals suppresses de-trapping via traps. In addition, the Si nanocrystals formed during the hydrogen plasma treatment can provide additional storage states.

Fig. 6(a) and (b) presents the endurance characteristics of control and standard samples under the pulse condition of $V_G - V_{fb} = \pm 7$ V for 10 ms. The flat-band voltage (V_{fb}) shift can be defined by using the C–V hysteresis under ±7 V gate voltage operation. The memory of control samples can be distinguished after 10^6 program/erase cycles at room temperature; however, memory is degraded to about 57.5%, as shown in Fig. 6(a). This is because during the endurance test, carrier transport between nanocrystals and the substrate can damage the surrounding oxide.

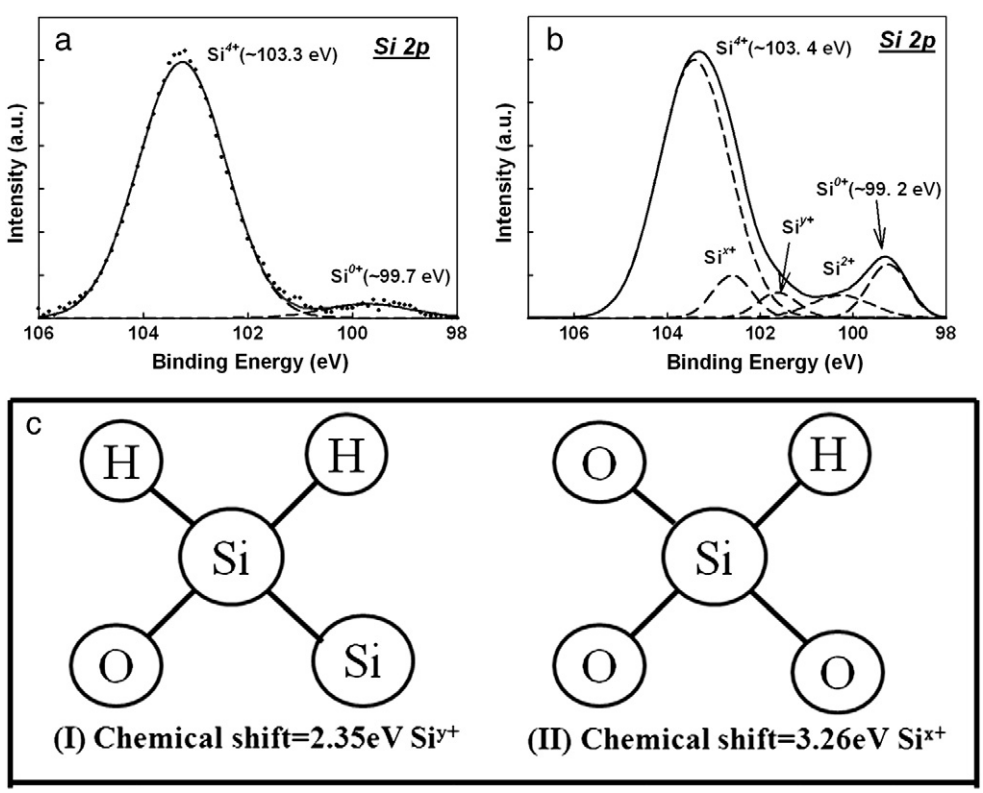

Fig. 3. XPS analysis of the Si 2p core-level spectrum. (a) Control sample, (b) standard sample, and (c) Si–H bond structure in the SiO_2 and theoretical chemical shifts calculated by the concept of local electronegativity.

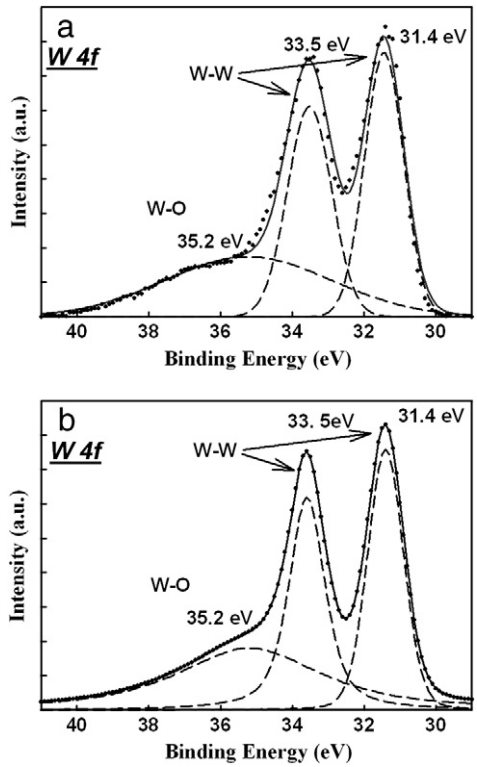

Fig. 4. XPS analysis of the W 4f core-level spectrum. (a) Control sample, and (b) standard sample.

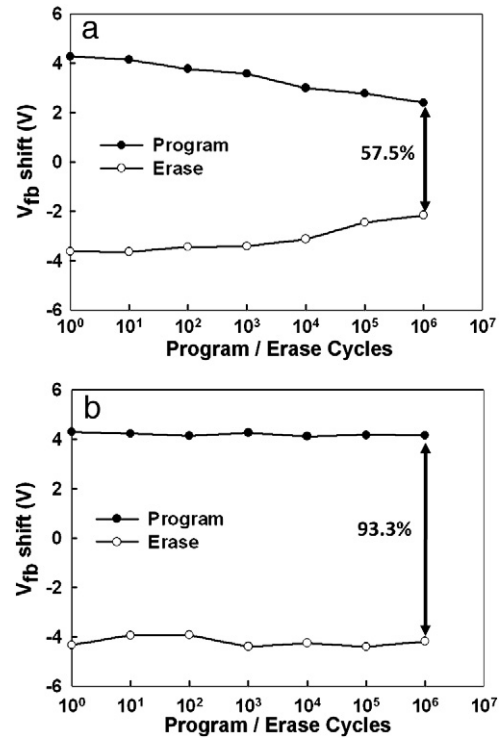

Fig. 6. Endurance characteristics of (a) control sample and (b) standard sample under the pulse condition of $V_G - V_{FB} = \pm 7$ V for 10 ms. The flat-band voltage can be defined by using the C–V hysteresis.

Fig. 6(b) shows that the variation of the memory window is stable ($\triangle V_{FB}$ of 93.3%) after 10^6 program/erase cycles for devices with the hydrogen plasma treatment. It is known that the $\triangle V_{FB}$ reduction during the endurance test is due to the degradation of the gate oxide [24]. The superior endurance characteristics of the sample with hydrogen plasma treatment can be attributed to the improvement of surrounding oxide quality. The surrounding oxide was strengthened by the hydrogen incorporation after the treatment; therefore, the generation rate of traps is reduced, resulting in better endurance properties.

Fig. 7 shows the retention characteristics of the W NC nonvolatile memory. The open triangles represent the standard sample, and the solid black circles represent the control sample. We used an extrapolation to give a long-term predictable result (dotted lines) after 1000 s (stable region of retention). The memory window significantly decays during the first 100 s due to the charge emission from the shallow traps in SiO*x* matrix to the substrate. However, after 100 s the memory window becomes more stable. A 1.39 V memory window (charge ratio remaining at 69.4%) can be obtained after 10^4 s. As shown in Fig. 6, the retention property of the sample with hydrogen plasma treatment is superior. The better retention characteristics of the sample with the plasma treatment can be attributed to the improvement of surrounding oxide quality.

As the density of NCs increases, the oxide surrounding those NCs becomes very thin. If the surrounding oxide quality is not sufficient, it will be unable to block the lateral electron migration effect, and the electron storage in the NCs will escape, as shown in Fig. 8(a). The hydrogen plasma treatment can be used to effectively passivate dangling bonds of the Si/SiO_2 interface and defects in the surrounding oxide such that Si–H bonds are formed. Hence, the lateral electron migration will be reduced, as shown in Fig. 8(b).

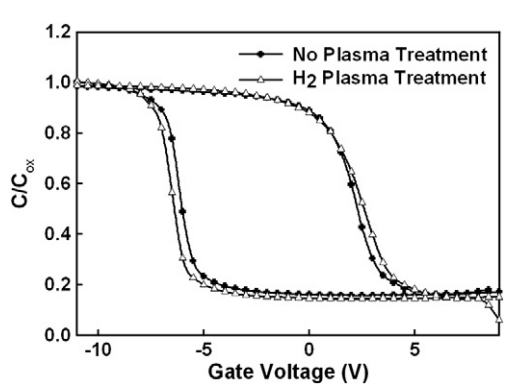

Fig. 5. Capacitance–voltage (C–V) hystereses of MOIOS structure with W nanocrystal NVM under ±10 V gate voltage operation.

4. Conclusion

This study investigates the influence of hydrogen plasma treatment on the electrical characteristics and the chemical composition of the proposed W nanocrystal nonvolatile memory. After the hydrogen plasma treatment, the XPS results indicate that Si dangling bonds (traps) in SiO_2 have been repaired by hydrogen passivation and have

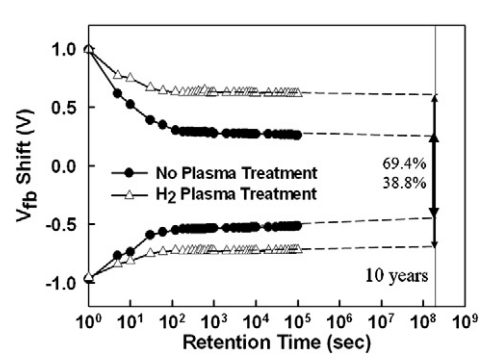

Fig. 7. Retention of the nonvolatile W nanocrystal NVM.

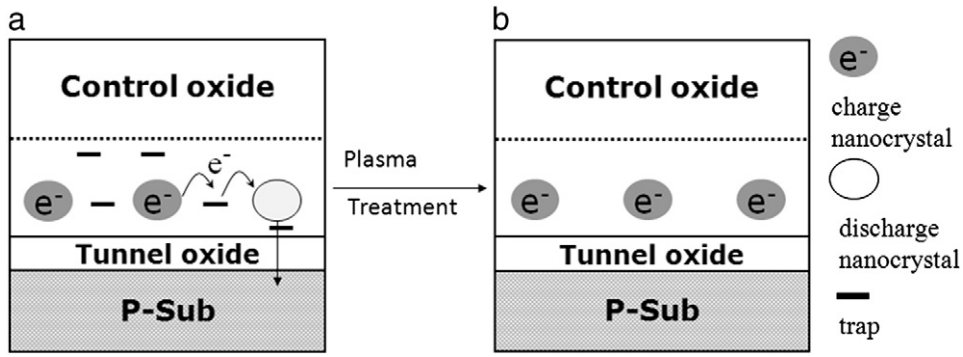

Fig. 8. (a) Lateral leakage current phenomenon of non-ideal NC structure. (b) NC structure with plasma treatment.

formed a H-passivated bonding (Si^{x+} and Si^{y+}). In addition, the binding energy reduction and the increased intensity of the Si^{0+} peak reveal that Si nanocrystals form due to the Si reduction from weak Si–O bonds during hydrogen plasma treatment. Because Si nanocrystals can provide additional storage centers, the memory window increases slightly, even though traps were passivated. By using the hydrogen plasma treatment, the endurance and retention properties of the memory device can be improved by 36% and 30%, respectively. The reason the reliability improved was that Si dangling bonds were repaired to form Si–H bonds during hydrogen plasma treatment. In addition, the process is compatible with current flash memory fabrication technology.

Acknowledgements

This work was performed at the National Science Council Core Facilities Laboratory for Nano-Science and Nano-Technology in Kaohsiung–Pingtung area and supported by the National Science Council of the Republic of China under Contract Nos. NSC-99-2120-M-110-001 and NSC 97-2112-M-110-009-MY3.

References

[1] H.E. Maes, J. Witter, G. Groeseneken, Proc. 17 European Solid State Devices Res. Conf. Bologna (1998) 157.
[2] S. Tiwari, F. Rana, K. Chan, H. Hanafi, C. Wei, D. Buchanan, IEEE Int. Electron Devices Meet Tech. Dig. (1995) 521.
[3] Chao-Cheng Lin, Ting-Chang Chang, Tu. Chun-Hao, Wei-Ren Chen, Hu. Chih-Wei, Simon M. Sze, Tseung-Yuen Tseng, Sheng-Chi Chen, Jian-Yang Lin, Appl. Phys. Lett. 93 (2008) 222101.
[4] Wei-Ren Chen, Ting-Chang Chang, Jui-Lung Yeh, Chun-Yen Chang, Shih-Ching Chen, Appl. Phys. Lett. 92 (2008) 062112.
[5] Wei-Ren Chen, Ting-Chang Chang, Jui-Lung Yeh, Simon M. Sze, Chun-Yen Chang, Uei-Shin Chen, Appl. Phys. Lett. 91 (2007) 222105.
[6] H.G. Yang, Y. Shi, S.L. Gu, B. Shen, P. Han, R. Zhang, Y.D. Zhang, Microelectron. J. 34 (2003) 71.
[7] C.H. Chen, T.C. Chang, I.H. Liao, P.B. Xi, Joe Hsieh, Chen Jason, Huang Tensor, S.M. Sze, U.S. Chen, J.R. Chen, Appl. Phys. Lett. 92 (2008) 013114.
[8] S.K. Samanta, Zerlinda Y.L. Tan, Won Jong Yoo, Ganesh Samudra, Sungjoo Lee, L.K. Bera, N. Balasubramanian, JVST B 23 (6) (2005) 2278.
[9] Jer-Chyi Wang, Pai-Chi Chou, Chao-Sung Lai, Wen-Hui Lee, Chi-Fong Ai, Microelectron. Reliab. 50 (2010) 639.
[10] M. Houssa, M. Tuominen, M. Naili, V. Afanas'ev, A. Stesmans, S. Haukka, M.M. Heyns, J. Appl. Phys. 87 (2000) 8615.
[11] W.R. Chen, T.C. Chang, P.T. Liu, P.S. Lin, C.H. Tu, C.Y. Chang, Appl. Phys. Lett. 90 (2007) 112108.
[12] G. Taraschi, S. Saini, W.W. Fan, L.C. Kimerling, J. Appl. Phys. 93 (2003) 9988.
[13] C.H. Tu, T.C. Chang, P.T. Liu, H.C. Liu, S.M. Sze, C.Y. Chang, Appl. Phys. Lett. 89 (2006) 162105.
[14] T. Suzuki, M. Muto, M. Hara, K. Yamabe, T. Hattori, Jpn. J. Appl. Phys. 25 (1986) 544.
[15] A. Ikeda, T. Sadou, H. Nagashima, K. Kouno, N. Yoshikawa, K. Tshukamoto, Y. Kuroki, Thin Solid Films 345 (1999) 172.
[16] Kazuhisa Sugiyama, Takayuki Igarashi, Kazunori Moriki, Yoshikatsu Nagasawa, Takayuki Aoyama, Rinshi Sugino, Takashi Ito, Takeo Hattori, Jpn. J. Appl. Phys. 29 (1990) L2401.
[17] T. Hattori, T. Igarashi, M. Ohi, H. Yamagishi, Jpn. J. Appl. Phys. 28 (1989) L1436.
[18] Yasushi Sawada, Noriyuki Taguchi, Kunihide Tachibana, Jpn. J. Appl. Phys. 38 (1999) 6506.
[19] Chung-Jin Kim, Sung-Jin Choi, Seong-Wan Ryu, Sungho Kim, Jae-Joon Chang, SuHak Bae, Byeong-Hyeok Sohn, Yang-Kyu Choi1, Nanotechnology 21 (2010) 125202.
[20] T.P. Nguyen, S. Lefrant, Phys. Condens. Matter (1989) 5197.
[21] L.G. Piper, W.T. Rawlins, J. Chem. Phys. 90 (1986) 320.
[22] R. Wolf, K. Wandel, Surf. Coat. Technol. 74 (75) (1995) 522.
[23] O. Kubaschewski, B.E. Hopkins, Oxidation of Metals and Alloys, Butterworths, London, 1953.
[24] P. Pavan, R. Bez, P. Olivo, E. Zanoni, Proc. IEEE 85 (1997) 1248.